

1 Electronic Supplementary Information (ESI)

2 **CO₂- and SO₂- tolerant dual phase composite membrane for oxygen separation**

3 S. Cheng^{a*}, M. Sogaard^a, L. Han^a, W. Zhang^b, M. Chen^a, A. Kaiser^a and P.V. Hendriksen^a

4 ^a *Department of Energy Conversion and Storage, Technical University of Denmark, Risø campus,*
5 *Frederiksborgvej 399, DK-4000 Roskilde, Denmark*

6
7 ^b *Department of Materials Science and Key Laboratory of Mobile Materials MOE, Jilin University,*
8 *130012 Changchun, China.*

9

10 *Corresponding author

11 Email: shic@dtu.dk

12

13

14

15

16

17

18

1 In the Experimental section, details of the synthesis and the characterization of the materials are presented,
2 followed by further details about the electrical and oxygen permeation flux measurements. Illustrations of the
3 experimental setups are included.

4 **1. Experimental details**

5 *1.1. Preparation of powders and membranes*

6 The starting materials used in the investigation were ZnO (99.9%, 200 mesh powder; Alfa-Aesar), γ -Al₂O₃
7 (99.5%, 40 nm to 80 nm APS powder; Alfa-Aesar), Ga₂O₃ (99.99%, 50 mesh powder; Alfa-Aesar), and
8 GCO10 powder (ultra-low surface area (ULSA) powder from Rhodia S.A., France).

9 For synthesis of the AGZO powder (Al_{0.02}Ga_{0.02}Zn_{0.96}O_{1.02}), γ -Al₂O₃ and Ga₂O₃ were mixed with ZnO at a
10 molar ratio of 1:1:96 (atomic ratio Al:Ga:Zn = 2:2:96) by roll milling for 24 h in ethanol using zirconia balls.
11 The resulting mixtures were then dried at room temperature for 24 hours followed by further drying at 130
12 °C for 3 h. The dried powders were calcined in an alumina crucible at 900 °C in N₂ for 5 hours. After
13 calcination, the powders were sieved using a mesh (U.S. Mesh 325), corresponding to mean particle
14 agglomerate-size of 48 μm. GCO10 powder was later mixed with as-prepared AGZO powder by ethanol
15 aided roll milling for 48 hours. The powder mixture consisted of 50 vol.% AGZO (Al_{0.02}Ga_{0.02}Zn_{0.96}O_{1.02}) and
16 50 vol.% GCO (Gd_{0.1}Ce_{0.9}O_{1.95-δ}), abbreviated as AGZO-GCO55. The final mixture was dried at 120 °C
17 overnight, followed by sieving using a mesh (U.S. Mesh 100). The 18 mm diameter membrane was prepared

1 by pressing the powder with a uniaxial pressure of 50 MPa followed by conducting an isostatic pressing at
2 60 MPa. The membrane was subsequently sintered at 1200 °C for 5 hours in air. The membrane was
3 polished by SiC sand paper and diamond paper to achieve a smooth and clean surface. The relative density
4 (geometrical) of the dual phase composite is close to 99% of the theoretical density (XRD). In order to
5 promote surface oxygen exchange, $\text{La}_{0.6}\text{Sr}_{0.4}\text{CoO}_{3-\delta}$ (LSC) porous activation layers were introduced by screen
6 printing an in-house developed pure LSC ink on both sides of the polished, dense membrane since LSC is a
7 good electrocatalyst for oxygen exchange reactions¹. The printed membrane was sintered at 900 °C to ensure
8 a good adhesion between the membrane and the catalytic layers.

9 ***1.2. Characterization of powders and membranes***

10 The powder XRD in this work was conducted on a Bruker Robot in Bragg-Brenano geometry with Cu K α in
11 a 2θ range of 20 °-90 °. *In-situ* XRD was carried out in a high temperature chamber from room temperature
12 to 900 °C. The powder of the crushed membrane is uniformly dispersed on a flat Pt foil that serves a sample
13 holder. The heating rate utilized in this work is 2 °C min⁻¹ and the XRD at each temperature was measured
14 before and after holding for 1 hour to ensure the chemical and thermal equilibrium. The XRD patterns were
15 indexed and compared by the data database of ICDD (International Centre for Diffraction Data) by the
16 software DIFFRAC plus. The morphology and chemical composition of the specimens in this work was
17 further investigated by a field emission gun scanning electron microscope (FEG-SEM) using a voltage of 20

1 kv. The high-resolution transmission electron microscopy (HRTEM) and scanning transmission electron
2 microscopy (STEM) images were performed using a JEM 3000F transmission electron microscope, operated
3 at 300 kV.

4 ***1.3. Electrical conductivity measurement***

5 The electrical conductivity measurement was conducted using a standard 4-terminal technique on a bar with
6 dimension $12 \times 0.8 \text{ cm} \times 0.8 \text{ mm}^3$. Prior to the measurement, the bar was polished with a SiC paper #1500.
7 Four Pt wires were ramped on separate spots of the bar. The electrical conductivity of the sample was
8 measured under a constant voltage (1 volt). The bar was mounted in a quartz tube in which the gas was
9 controlled by varying the gas flow around the sample. The oxygen partial pressure was monitored by a
10 zirconia sensor.

11 ***1.4. Investigation of powders annealed in CO₂ and SO₂ containing atmospheres***

12 The material stability was investigated both by membrane test in flowing gas and in material exposure tests
13 of the crushed powder materials as further outlined below.

14 Annealing the powder in CO₂ and SO₂ at high temperature was carried out using a tube furnace allowing
15 control of the gas atmosphere. The flow of CO₂ was monitored by a ball flowmeter. For the pretreatment of
16 the powders in SO₂, Al₂(SO₄)₃ powder was placed in a crucible and covered by a thin layer of super wool.

17 Fresh powders of AGZO-GCO55 and La_{0.6}Sr_{0.4}FeO_{3-δ}-Gd_{0.1}Ce_{0.9}O_{1.95-δ} (internal standard) were dispersed on

1 the super wool and the crucible was heated inside the tube furnace. Air is flowed for circulation. Upon
2 heating, the $\text{Al}_2(\text{SO}_4)_3$ decomposes exposing the candidate materials to a high SO_2 activity. The generation of
3 SO_2 by the thermal decomposition of $\text{Al}_2(\text{SO}_4)_3$ was confirmed by an external mass spectrometer.

4 ***1.5. Oxygen permeation measurement***

5 Oxygen permeation measurements were performed in an in-house built rig displayed in Fig. S 1. The
6 membrane with a thickness of approximately 1.1 mm and a diameter of 15 mm was initially sealed between
7 two alumina tubes with a 30/70 vol.% MgO/sodium aluminosilicate glass composite. The membrane was
8 placed in the middle zone of a height adjustable tube furnace. The feed side tube below the membrane was
9 supplied with gas from the feed side manifold which has a feed gas inlet and outlet. Similarly, the permeate
10 side of the membrane was purged with gas from an “anode” manifold. The feed side was flushed with air/ O_2
11 with a constant flow rate of 100 Nml min^{-1} and the permeate side was flushed with various flows of N_2/CO_2 .
12 The flow of gases was monitored by mass flow controllers (See Fig. S 2). The net oxygen permeation flux
13 can be deduced from the $p\text{O}_2$ difference between inlet and outlet gases flowing through the permeate side.
14 The $p\text{O}_2$ is precisely monitored by two in-house built YSZ-based oxygen sensors. The oxygen permeation
15 flux of the membrane may be written

$$J_{O_2} = \frac{\dot{N}(pO_2^{out} - pO_2^{in})}{A} \quad \text{Equation 1}$$

- 1 Where A is the net area of the permeate side of the membrane, pO_2^{in} and pO_2^{out} denote oxygen partial
 2 pressure of inlet and outlet, respectively. \dot{N} represents the mass flow rate of outlet gases. The oxygen partial
 3 pressures are calculated *via* the Nernst equation from the Emf's measured with the zirconia sensors.

$$E = \frac{RT}{4F} \ln \frac{pO_2}{pO_{2,ref}} \quad \text{Equation 2}$$

- 4 Where E is the open circuit voltage of the oxygen sensor. R is the gas constant. $pO_{2,ref}$ is the oxygen partial
 5 pressure at reference electrode which retains at 0.21 bar, T is the temperature of the sensor.
- 6 The leak in the system was assessed by means of a mass flow meter on the permeate stream. When a perfect
 7 sealing is achieved, the outlet gas flow rate should be equivalent to the inlet flow. If there are leaks in the
 8 membrane or pinholes or cracks in the glass encapsulation, the flow rate of the outlet gas will be lower than
 9 that of the inlet gas. Typically, in the cases where a significant leak is observed during the permeation
 10 measurement, a thermally activated increase in oxygen flux is not observed. In the data reported here the
 11 inlet and outlet flows are within the uncertainty (1%) identical and a thermal activated oxygen permeation
 12 flux was observed, indicating a perfect sealing. The maximum leak originating from pinholes in the sealant

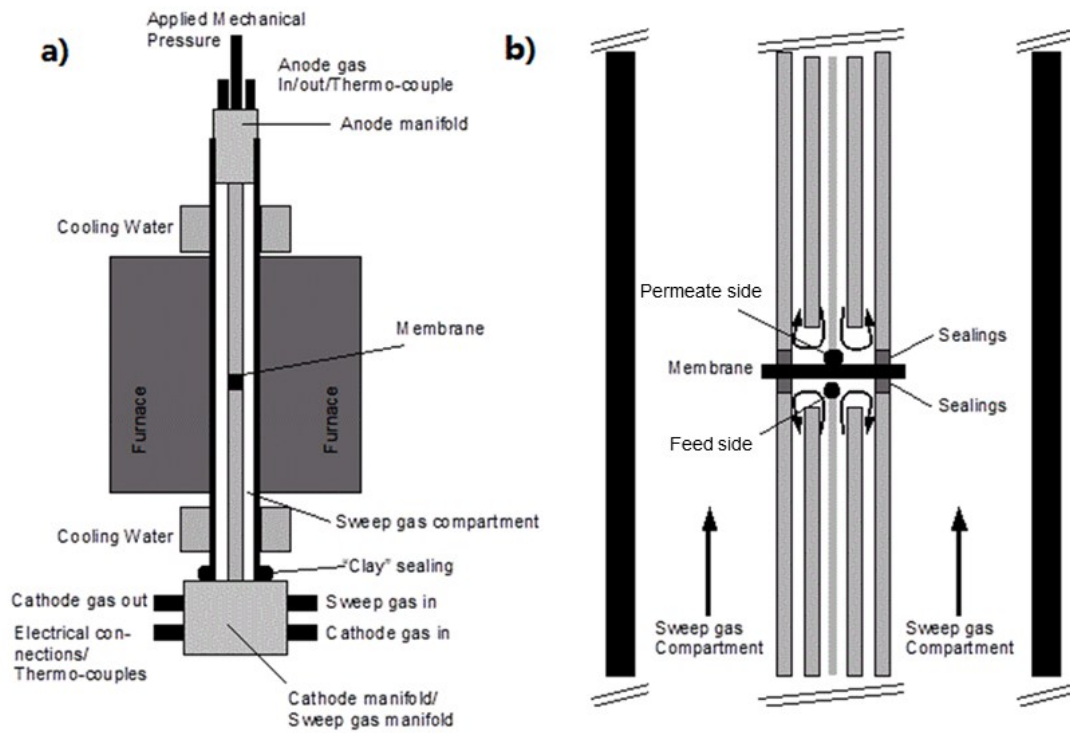
1 and due to other sources of oxygen in the permeate flow through the membrane is estimated to be lower than
2 5% at low temperature (600 °C) based on the gas sensor. Below 600 °C a large leak arises due to thermal
3 expansion mismatch driven failure at the sealant. We check a worst case estimate of leakage flux in each
4 membrane based on the lowest flux during cooling (<600 °C), before an obvious compromise of the seal is
5 detected. This was indicated by a sudden drop of measured voltage of pO₂ outlet sensor which typically
6 occurs at temperatures between 400 °C and 600 °C. The worst leakage was subtracted from the measured
7 flux to ensure an underestimated resulting flux. The worst leakage fluxes for each measurement were listed
8 in Table S1.

9 **Table S1. Estimated worst leakage for each membrane**

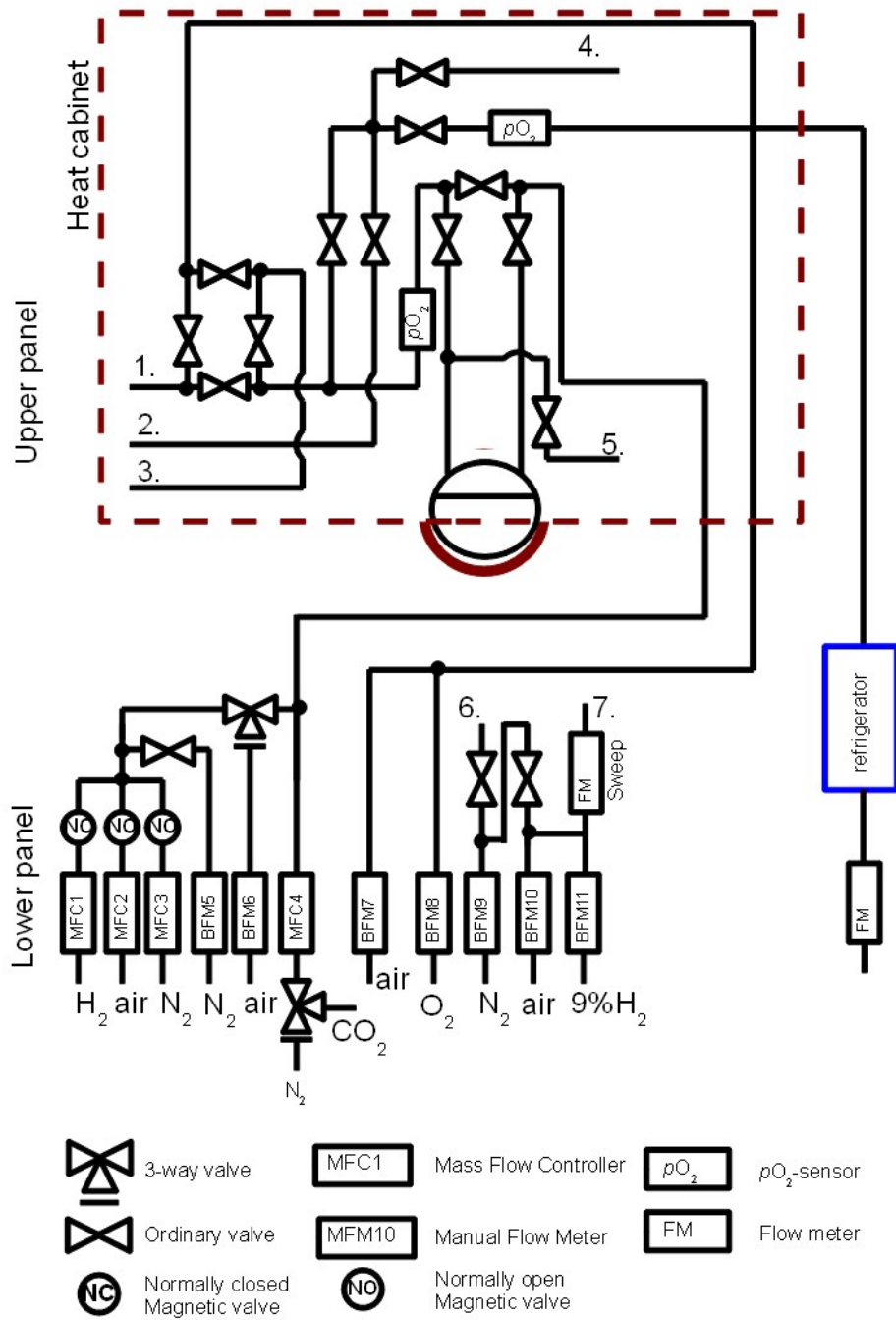
Membrane	$J_{O_2, leak} / \text{mol cm}^{-2} \text{ min}^{-1}$	% difference of $J_{O_2, leak}$ from J_{O_2} at 900 °C
GCO-AGZO55 with LSC coating	2.08×10^{-9}	1%
GCO-AGZO55 without LSC coating	1.99×10^{-9}	17%

10

11 Furthermore, the peak for N₂ arising from the leak from ambient air through the membrane or the sealing
12 cannot be observed by an Agilent 490 micro gas chromatograph during the test, further demonstrating the
13 gas tight during the permeation measurements.



1
 2 Fig. S 1 a) Schematic illustration of the membrane test rig. b) Zoom into the heated part of the
 3 membrane test rig.



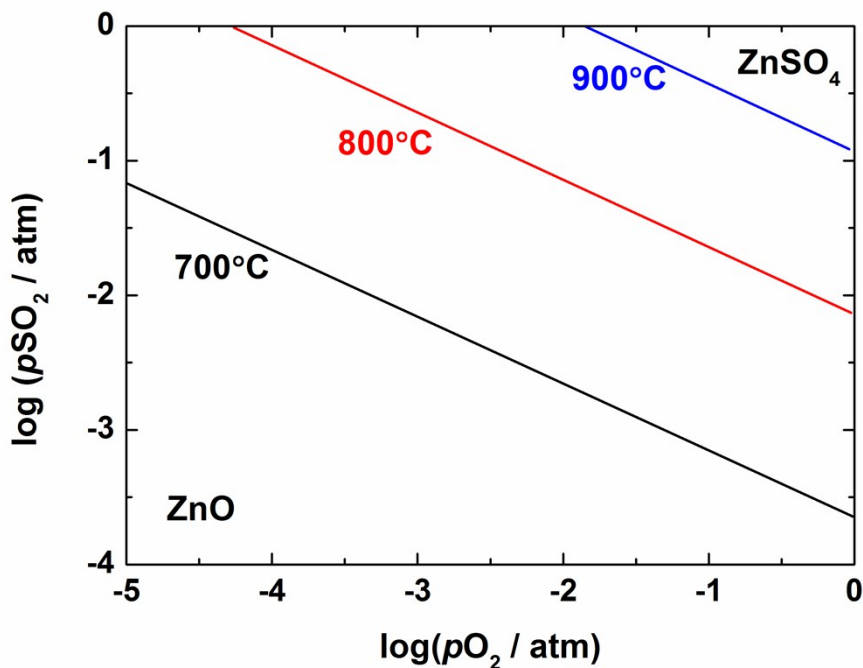
1

2 Fig. S 2 Flow diagram of the upper and lower panel and outlet through refrigerator and flow meter .
 3 The numbers in the diagram represents the following 1. Gas to the permeate side of the membrane
 4 (typically the reducing side) 2. Gas from the permeate side of the membrane. 3. Gas to the feed side of
 5 the membrane. 4. Gas to refrigerator and flow meter 5. N/A 6. Gas outlet for further extensions of the
 6 rig, 7. Gas to the sweep gas compartment.

7

1 **2. Additional results**

2 Fig. S 3 shows the calculated phase diagram of Zn-S-O at 700-900 °C as functions of p_{O_2} and p_{SO_2} . The
3 calculations were carried out using the FACTSAGE Thermochemical Software and Databases². $ZnCO_3$ will
4 completely decompose to ZnO and CO_2 above 200 °C. The lines mark the phase boundary, illustrating the
5 combination of p_{O_2} and p_{SO_2} where $ZnSO_4$ may form at 700 °C, 800 °C and 900 °C. The upper part of the
6 phase boundary demonstrates the atmosphere for $ZnSO_4$ and the lower part corresponds to the condition for a
7 stable ZnO .

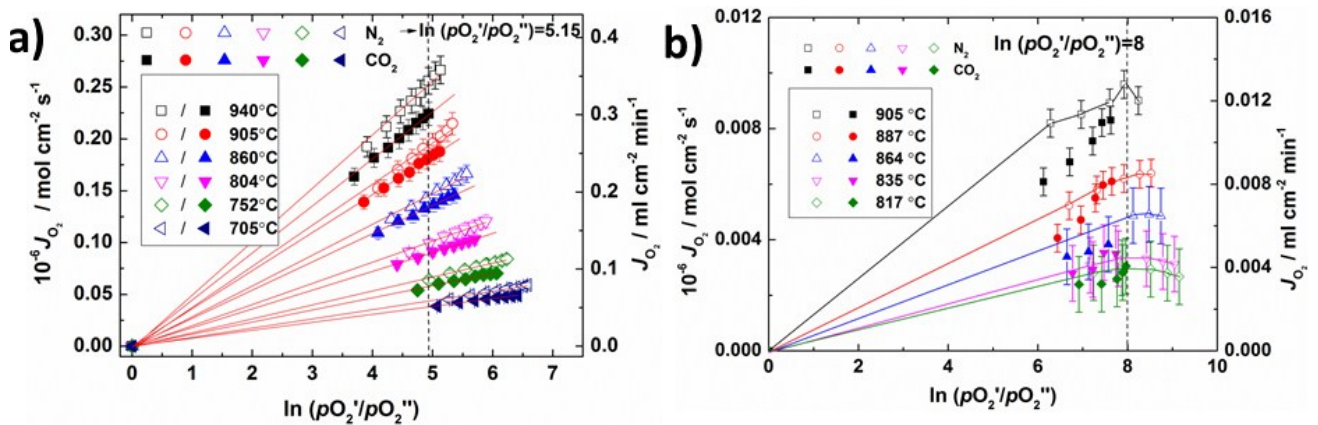


8

9 **Fig. S 3 Calculated phase diagram as functions of logarithm oxygen partial pressure and sulfur**
10 **dioxide partial pressure at 700 °C, 800 °C and 900 °C.**

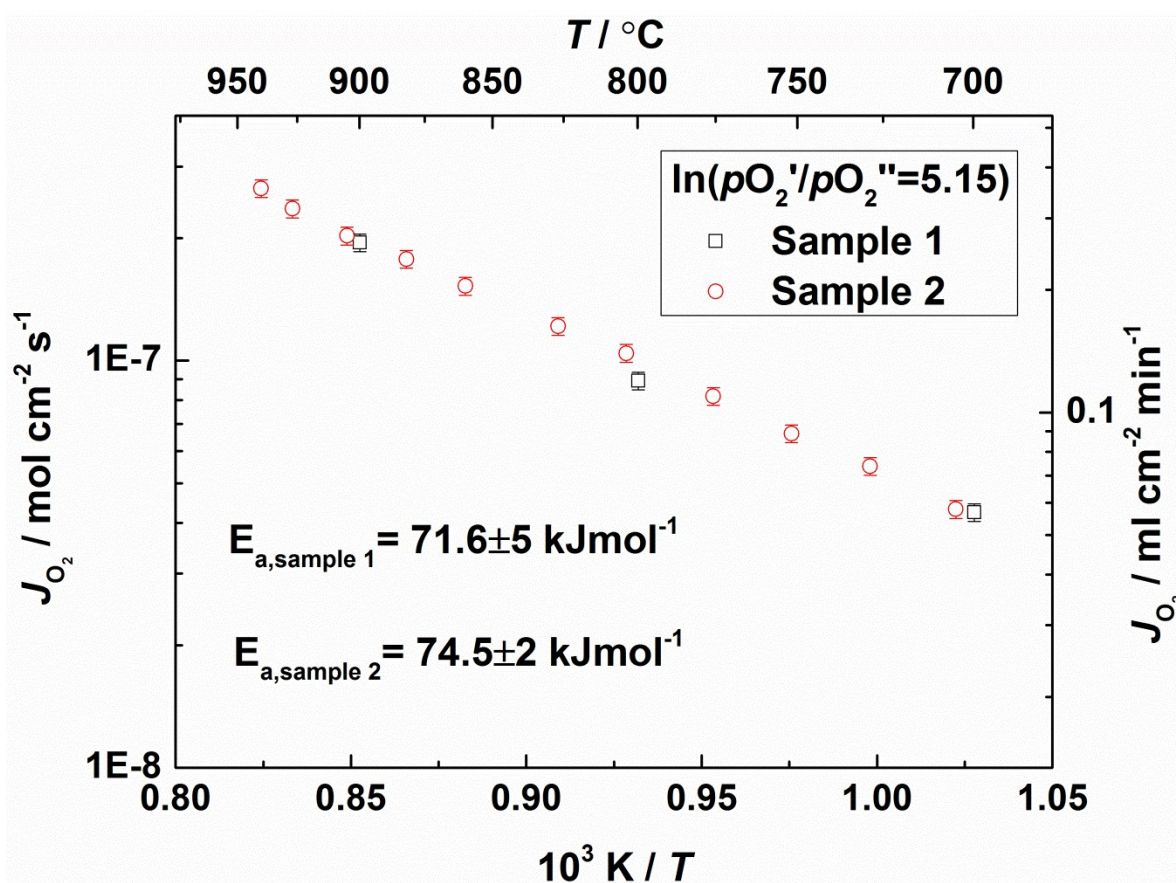
1 Fig. S 4 shows the oxygen flux of AGZO-GCO5 membrane with and without LSC coating as a function of \ln
 2 (pO_2'/pO_2'') when using either N_2 or CO_2 as the sweep gas in the temperature range 705-940 °C. The red
 3 lines in Fig. S4 a) are a linear fit to the results. The solid lines in Fig. S4 b) are plotted as a guide to the eye.
 4 The vertical dashed line is the fluxes at a fixed driving force from which the Arrhenius curves (Fig. 3 in the
 5 main article) are obtained. The linear fit follows the Wagner equation for calculating bulk diffusion
 6 controlled flux:

$$J_{O_2} = \frac{RT\sigma_{amb}}{16F^2L} \ln \frac{pO_2'}{pO_2''} \quad \text{Equation 3}$$



8 Fig. S 4 Oxygen permeation flux J_{O_2} through a 1.1 mm thick AZGO-GCO55 composite membrane a)
 9 with and b) without LSC coating as a function of the natural logarithm of the ratio between the oxygen
 10 partial pressure on feed and the permeate side. N_2 (hollow) and CO_2 (fill) were used as sweep gas,
 11 respectively.

- 1 As shown in Fig. S 5, permeation flux measurements for two nominally identical membranes were also
- 2 carried out. The difference between the fluxes is less than 5% illustrating very good reproducibility. The
- 3 largest uncertainty on the flux values originates from the estimation of the surface area.



4

5 **Fig. S 5 Arrhenius plot of the oxygen permeation flux (J_{O_2}) of two nominally identical AGZO-GCO55**

6 **membranes (Sample 1 and 2) measured in N_2 on the permeate side under a fixed driving force (\ln**

7 **$(p_{O_2}'/p_{O_2}''=5.15)$ as a function of inverse absolute temperature.**

8 Several studies report on the oxygen permeability of various composites based on doped ceria as the ionic

9 conducting phase. Selected results are summarized in Table S. 1 together with the oxygen flux results of the

1 AGZO-GCO55 membrane reported in this work. The AGZO-GCO55 membranes virtually display oxygen
 2 permeation fluxes comparable to literature¹. It should be noted that the electronic conductors used in the
 3 studies in the literature either contain relatively expensive metals (Ag), toxic elements (Cr, Ni and Co) or
 4 alkaline earth elements (Sr). For the economical comprehensiveness of the technology expensive and toxic
 5 elements should be avoided. For alkaline earth elements containing electronic conductors, the stability of
 6 these materials in CO₂ and SO₂ is problematic. AGZO-GCO55 avoids the use of toxic, expensive and
 7 alkaline earth elements.

8 **Table S.2 Oxygen permeation fluxes of dual phase composites involving doped ceria. The values**
 9 **represent volume percent of each phase.**

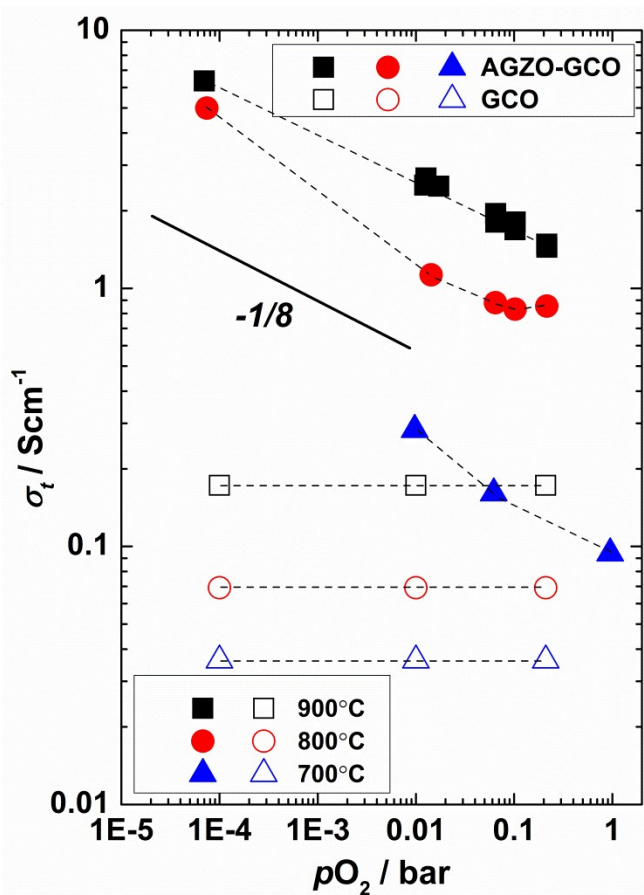
Membrane	T (°C)	J_{O_2} (mol cm ² s ⁻¹)	Thickness (mm)	pO ₂ ^l /pO ₂ ^h	Ref.
*Gd _{0.1} Ce _{0.9} O _{2-δ} (60)/NiFe ₂ O ₄ (40)	900-1000	7.93×10 ⁻⁸ -2.28×10 ⁻⁷	0.5	Air/He,Ne	3
*Gd _{0.1} Ce _{0.9} O _{2-δ} (60)/NiFe ₂ O ₄ (40)	900-1000	6.79×10 ⁻⁸ -2.05×10 ⁻⁷	0.5	Air/He,Ne	3
Sm _{0.15} Ce _{0.85} O _{1.925} (75)/ Sm _{0.6} Sr _{0.4} FeO _{3-δ} (25)	750-940	1.7×10 ⁻⁷ -5.92×10 ⁻⁷	0.5	Air/He	4
Sm _{0.15} Ce _{0.85} O _{1.925} (75)/ Sm _{0.6} Sr _{0.4} CrO _{3-δ} (25)	750-940	5.87×10 ⁻⁸ -2.00×10 ⁻⁷	0.5	Air/He	4
Tb _{0.2} Ce _{0.9} O _{2-δ} (60)/NiFe ₂ O ₄ (40)	800-1000	2.84×10 ⁻⁸ -1.51×10 ⁻⁷	0.68	Air/CO ₂	5
Gd _{0.1} Ce _{0.9} O _{2-δ} (84)/Ag-CuO (16)	600-890	1.12×10 ⁻⁸ -2.20×10 ⁻⁷	1.1	Air/N ₂	6
Gd _{0.2} Ce _{0.9} O _{2-δ} (48)/La _{0.8} Sr _{0.2} Fe _{0.8} Co _{0.2} O _{3-δ} (52)	950	6.3×10 ⁻⁸	1.0	Air/He	7
Gd _{0.2} Ce _{0.9} O _{2-δ}	950	9.94×10 ⁻¹⁰	1.35	Air/Ar	7
Gd _{0.1} Ce _{0.9} O _{2-δ} (50)/Al _{0.02} Ga _{0.02} Zn _{0.96} O _{1.02} (50)	700-940	4.36×10 ⁻⁸ -2.67×10 ⁻⁷	1.1	Air/N ₂	This work
Gd _{0.1} Ce _{0.9} O _{2-δ} (50)/Al _{0.02} Ga _{0.02} Zn _{0.96} O _{1.02} (50)	700-940	3.94×10 ⁻⁸ -2.33×10 ⁻⁷	1.1	Air/CO ₂	This work

10 *weight percent

11

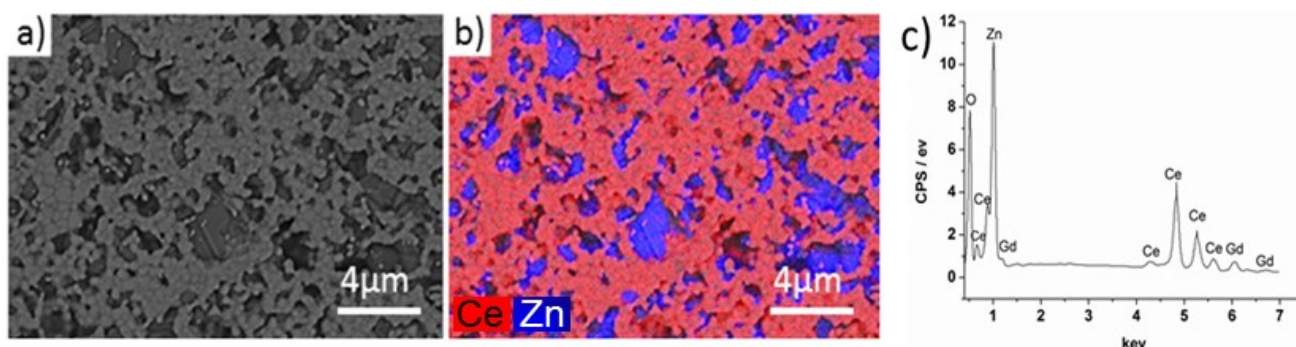
¹ This is to be expected as in absence of relation between the two phases the flux in these systems should be limited by the ionic conductivity of ceria.

1 Fig. S 6 shows the total conductivity of AGZO-GCO55 and GCO10 as a function of oxygen partial pressure
 2 at 700 °C, 800 °C and 900 °C, respectively. The total conductivity of AGZO-GCO55 is more than one order
 3 of magnitude larger than that of GCO, indicating that the total conductivity of the composite is dominated by
 4 the percolating AGZO phase. In addition, it can be observed that as the oxygen partial pressure decreases the
 5 electronic conductivity increases, illustrating a behavior of *n*-type electronic conductivity, which is
 6 consistent with literature^{8,9}.



7
 8 **Fig. S 6** Logarithm total conductivity of AGZO-GCO (solid symbols) and GCO¹⁰ (open symbols) as a
 9 function of logarithm oxygen partial pressure. Dotted lines are plotted as a guide to the eye.

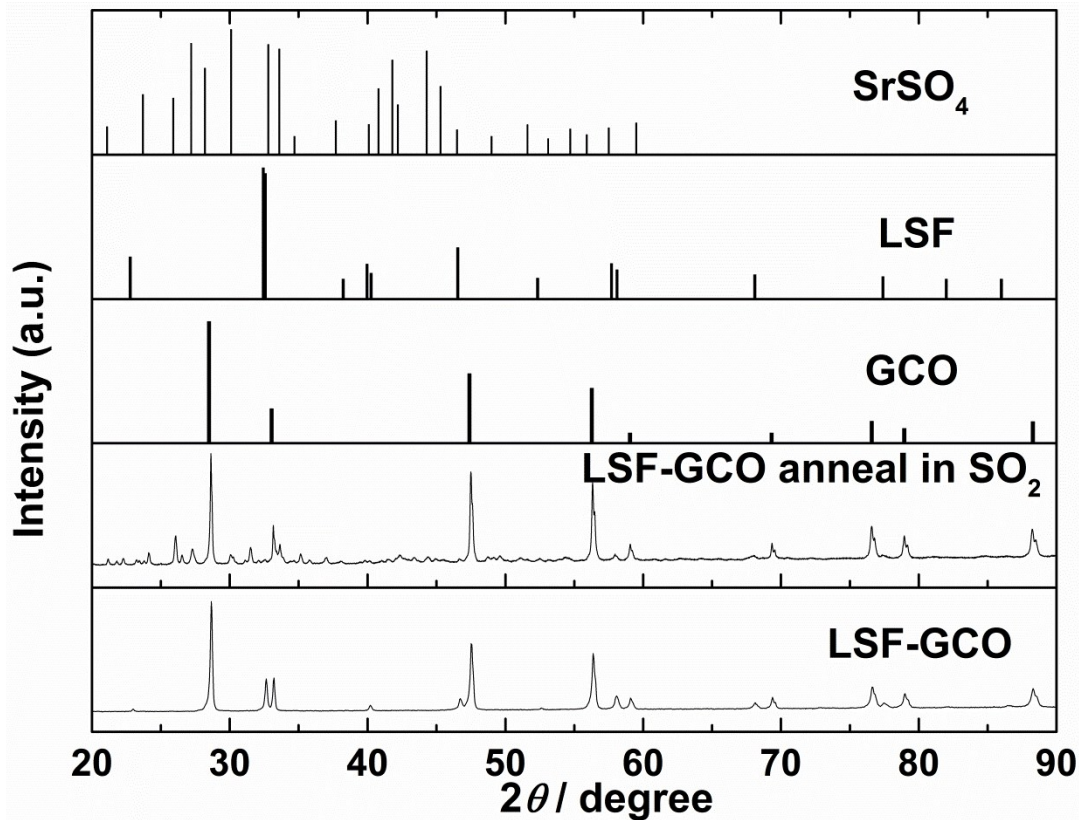
1 Fig. S 7 shows a SEM micrograph of a polished and thermally etched (1200°C for 0.5 hour) polished
2 membrane disk. A distinct separation of the two phases can be clearly observed. The average grain size for
3 both phases is less than 4 μm. The homogenous distribution of the two phases yields a good percolation for
4 both phases.



5
6 **Fig. S 7 a) BSEM micrograph of a polished and thermally etched membrane b) EDX mapping**
7 **micrograph Ce (red), Zn (blue) c) EDX spectrum**

8 Fig. 1 (main manuscript) shows the XRD patterns of powders of GCO-AGZO55 annealed in a SO₂
9 containing atmosphere. A powder of 50 vol. % Gd_{0.1}Ce_{0.9}O_{1.95-δ} -50 vol. % La_{0.6}Sr_{0.4}FeO_{3-δ} (GCO-LSF55),
10 which serves as an internal standard, was annealed together with AGZO-GCO55 for the same experimental
11 condition.

12 Fig. S 8 shows the XRD patterns of LSF-GCO55 annealed in the SO₂ containing atmosphere at 850 °C for 2
13 hours. For the LSF-GCO composition SrSO₄ could be detected while for ZnO no formation of sulfates could
14 be observed (see Fig. 1). The reaction between Sr and SO₂ is also reported for La_{0.6}Sr_{0.4}Co_{0.8}Fe_{0.2}O_{3-δ} samples
15 annealed in SO₂ above 800 °C¹¹.

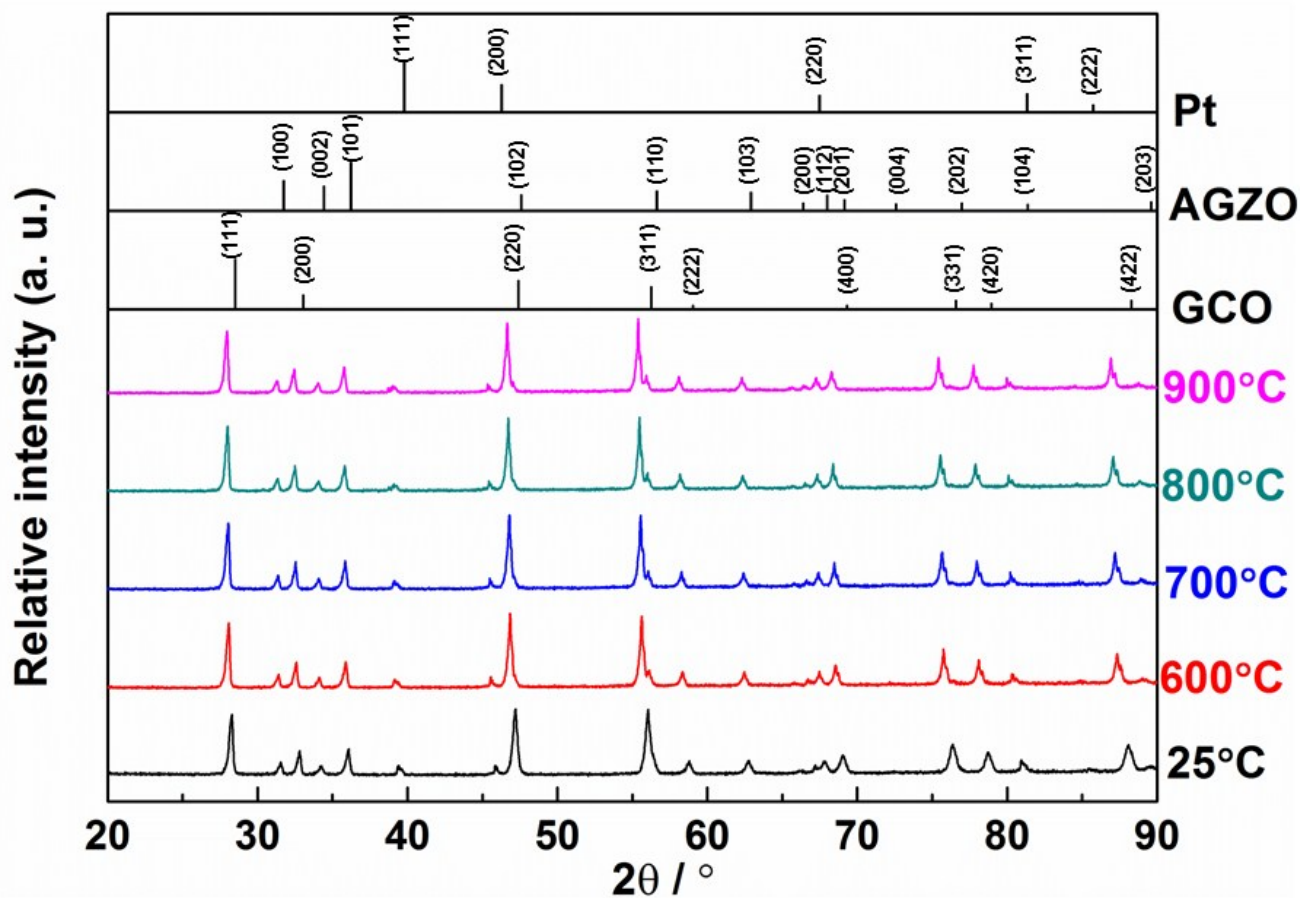


1

2 Fig. S 8 XRD patterns of CGO-LSF55 dual-phase composite membrane annealed in SO₂ at 850 °C for
 3 2 hours.

4 Fig. S 9 shows *in-situ* XRD patterns of a powder of crushed AGZO-GCO55 dual phase membrane in the
 5 temperature range of 30-900 °C obtained in air. The peaks corresponding to AGZO, GCO and Pt are present
 6 up to 900 °C. No other peaks could be detected, illustrating the phase stability of AGZO and GCO at high
 7 temperature.

8



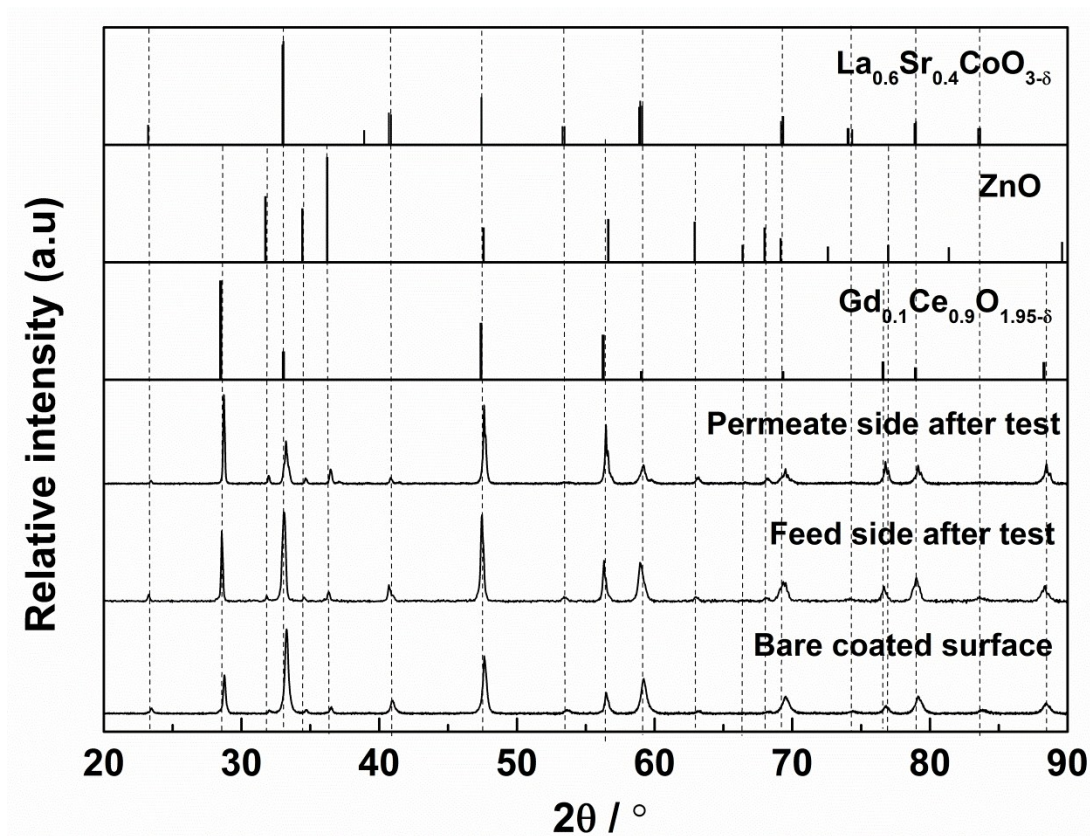
1

2 **Fig. S 9 *In-situ* XRD patterns of CGO-AZGO55 composites at elevated temperature. Dwell time at**
 3 **each temperature was 1 hour to reach steady state. The XRD data collection last for 1 hour at each**
 4 **temperature. The sample holder is a Pt foil.**

5 Fig. S 10 shows XRD patterns of the surfaces of pre-test AGZO-GCO55 with a LSC catalytic layer and feed
 6 side as well as permeate side of AGZO-GCO55 with LSC layer after permeation measurement. For the feed
 7 side, no obvious change of the peaks can be observed after test. Compared to the pre-test XRD patterns and
 8 the feed side pattern, the intensity of LSC peaks of the permeate side is lower and the width of the peaks is

1 broadening. The reason for the change of the peaks will be further discussed in conjunction with the results

2 of SEM-EDX.



3

4 Fig. S 10 Normalized XRD patterns of an AGZO-GCO dual phase membrane with LSC64 catalytic

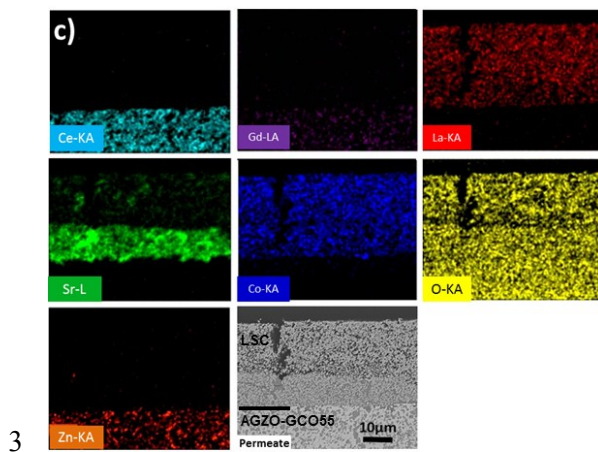
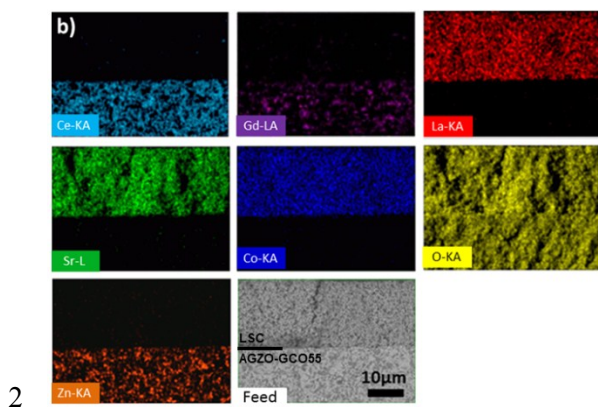
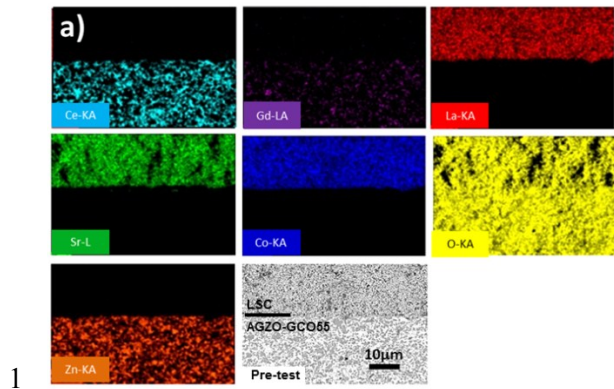
5 layers on both side before and after test. Zero shifts of 0.23°, 0.10° and 0.30° (arising from the XRD

6 system) of permeate side “after test”, feed side “after test” and bare coated surface respectively, are

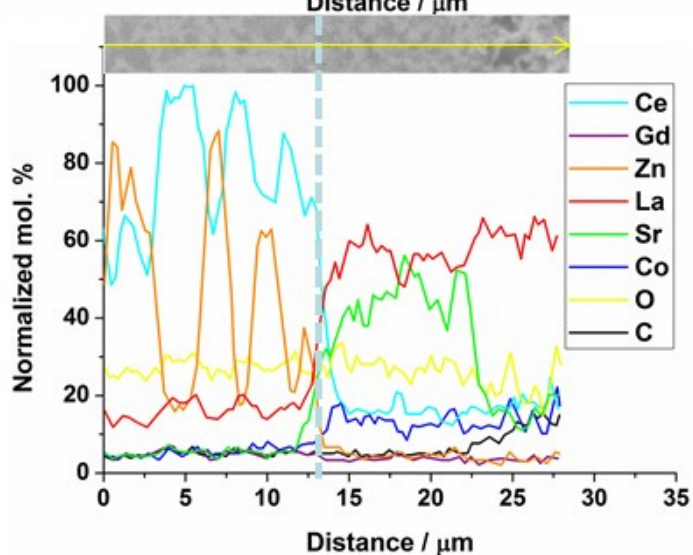
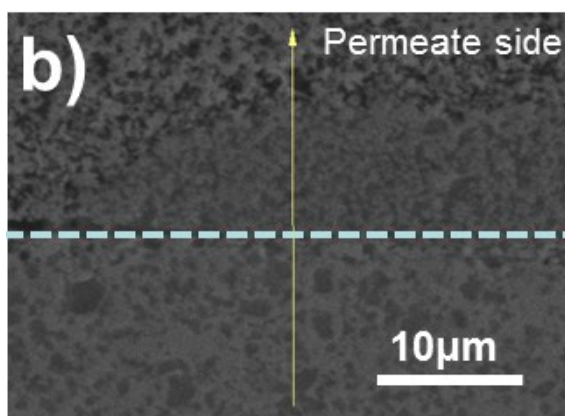
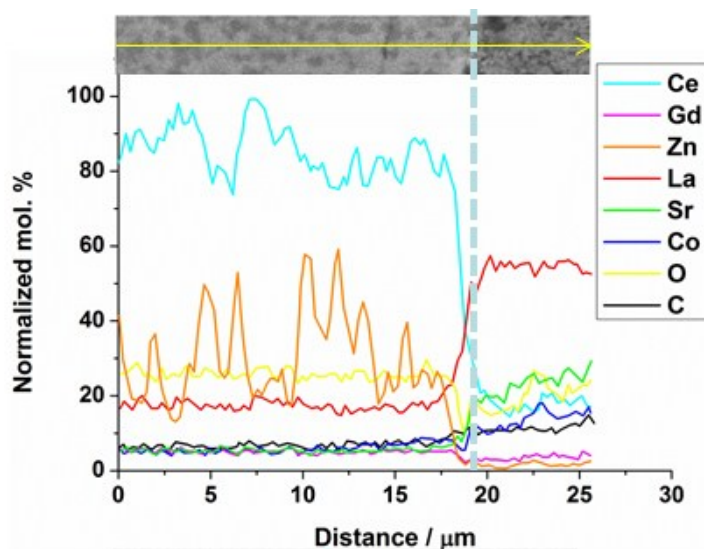
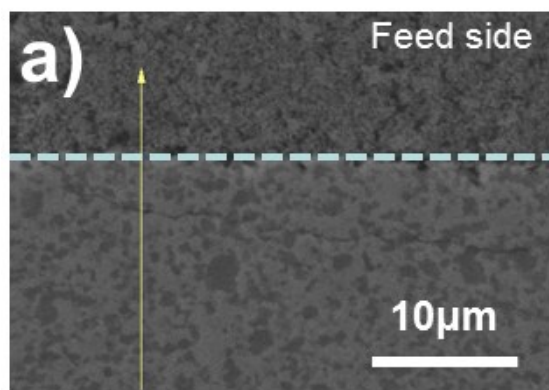
7 corrected for.

8

1 Fig. S 11 a) shows SEM elemental mapping of the cross section of a pre-test AGZO-GCO55/LSC interface.
2 For the pre-test AGZO-GCO55/LSC interface, no trace of cation diffusion or reaction can be detected. Fig. S
3 11 b) and c) shows elemental mapping of the same interface after test for the feed and permeate side,
4 respectively. Fig. S 12 a) and b) show line scans of the AGZO-GCO55/LSC interface of the feed and
5 permeate side after measurement, respectively. It can be seen that the concentration of Sr is pronouncedly
6 increased in a 10 μm thick layer adjacent to the membrane on the permeate side. Segregation of Sr can occur
7 in Sr-doped perovskite based cathodes at high temperatures and is found to significantly inhibit the oxygen
8 reduction reaction.¹²⁻¹⁵ According to thermodynamic calculation, LSC is more likely to react with CO_2 in
9 high $p\text{O}_2$. Therefore, SrCO_3 arising from the reaction between SrO and CO_2 has formed closest to the
10 interface where the $p\text{O}_2$ is higher than in the gas stream. Sr from the rest of the electrode has in turn diffused
11 towards the interface. Upon re-oxidation/cooling in N_2 the perovskite forms again with a high Sr content
12 perovskite adjacent to the membrane. The variation of the Sr content can also be seen from the peak
13 broadening in the XRD pattern (See Fig. S 10).



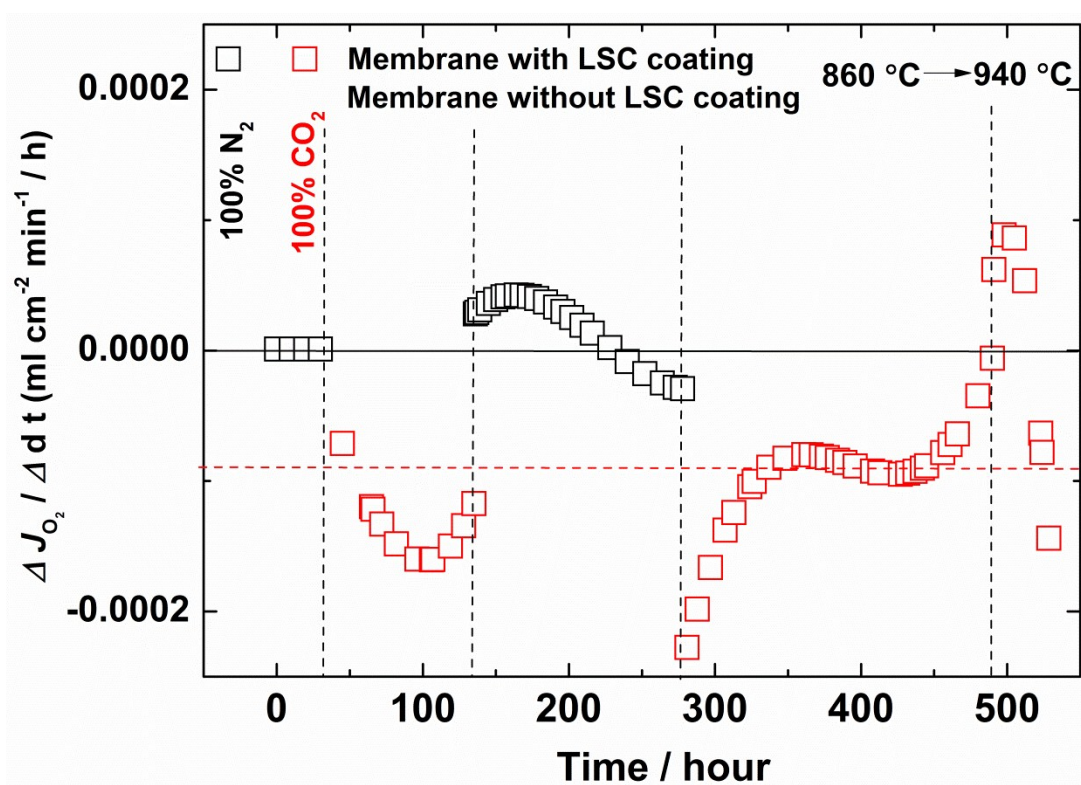
4 Fig. S 11 BSEM and EDX elemental mapping micrographs of the interfaces between the AGZO-
 5 GCO55 membrane and the LSC catalytic layer: a) pre-test interface b) Feed side interface after
 6 measurement c) permeate side interface after measurement (involving aging test in CO₂).



1
 2 **Fig. S 12 EDX line scans for La, Sr, Co, Gd, Ce, Zn, O, C taken along the green arrow starting from**
 3 **the AGZO-GCO membrane and passing across AGZO-GCO/LSC interface : a). Feed side b).**
 4 **Permeate side.**

5 Fig. S 13 displays the degradation rate of the membrane as a function of time, which is obtained by taking
 6 the derivative of oxygen permeation flux versus time. In general, the degradation rate when using N₂ as the
 7 sweep gas is scattering in the range of $\pm 5 \times 10^{-6}$ ml cm⁻² min⁻¹/ h, which is negligible. It indicates that the flux

1 is extremely stable when using 100% N₂ as the sweep gas. Notice that the degradation rate when using 100%
 2 CO₂ as the sweep gas is about -2×10^{-4} ml cm⁻² min⁻¹ / h at the beginning, followed by a decreased rate
 3 subsequently leveling off. This shows that the flux degrades in CO₂, but with a continuously decreased rate
 4 (860 °C). With respect to the membrane without LSC coating measured using 100% CO₂ as the sweep gas,
 5 the flux increases as a function of time following the rate of 3×10^{-5} ml cm⁻² min⁻¹ / h.



6
 7 **Fig. S 13** The degradation rate of the oxygen permeation fluxes of the membrane with and without
 8 LSC coating as a function of time. The results are calculated by taking the derivative of flux vs. time
 9 (See Fig. 4 in the main article)

1 References

- 2 1. M. Søgaaard, P. V. Hendriksen, M. Mogensen, F. W. Poulsen and E. Skou, *Solid State Ionics*, 2006,
3 **177**, 3285-3296.
- 4 2. C. W. Bale, P. Chartrand, S. A. Degterov, G. Eriksson, K. Hack, R. Ben Mahfoud, J. Melançon, A.
5 D. Pelton and S. Petersen, *Calphad*, 2002, **26**, 189-228.
- 6 3. H. Luo, K. Efimov, H. Jiang, A. Feldhoff, H. Wang and J. Caro, *Angew. Chem. Int. Ed.*, 2011, **50**,
7 759-763.
- 8 4. X. Zhu, M. Li, H. Liu, T. Zhang, Y. Cong and W. Yang, *Journal of Membrane Science*, 2012, **394–**
9 **395**, 120-130.
- 10 5. M. Balaguer, J. García-Fayos, C. Solís and J. M. Serra, *Chem. Mater.*, 2013, **25**, 4986-4993.
- 11 6. A. J. Samson, M. Søgaaard and P. V. Hendriksen, *J. Membr. Sci.*, 2014, **470**, 178-188.
- 12 7. V. V. Kharton, F. M. Figueiredo, L. Navarro, E. N. Naumovich, A. V. Kovalevsky, A. A.
13 Yaremchenko, A. P. Viskup, A. Carneiro, F. M. B. Marques and J. R. Frade, *Journal of Materials*
14 *Science*, 2001, **36**, 1105-1117.
- 15 8. S. Erdal, C. Kjølseth and T. Norby, *The Journal of Physical Chemistry C*, 2010, **114**, 16785-16792.
- 16 9. T. S. Bjørheim, S. Erdal, K. M. Johansen, K. E. Knutsen and T. Norby, *The Journal of Physical*
17 *Chemistry C*, 2012, **116**, 23764-23772.
- 18 10. S. Wang, T. Kobayashi, M. Dokiya and T. Hashimoto, *J. Electrochem. Soc.*, 2000, **147**, 3606-3609.
- 19 11. J. Gao, L. Li, Z. Yin, J. Zhang, S. Lu and X. Tan, *Journal of Membrane Science*, 2014, **455**, 341-348.
- 20 12. M. Kubicek, A. Limbeck, T. Frömling, H. Hutter and J. Fleig, *Journal of The Electrochemical*
21 *Society*, 2011, **158**, B727-B734.
- 22 13. V. I. Sharma and B. Yildiz, *Journal of The Electrochemical Society*, 2010, **157**, B441-B448.
- 23 14. P. Hjalmarsson, M. B. Mogensen and M. Søgaaard, *Solid State Ionics*, 2008, **179**, 1422-1426.
- 24 15. E. Bucher, W. Sitte, F. Klauser and E. Bertel, *Solid State Ionics*, 2012, **208**, 43-51.